INORGANIC CHEMISTRY
FRONTIERS

RESEARCH ARTICLE

View Article Online
View Journal





Cite this: DOI: 10.1039/d3qi00841j

# An endoplasmic reticulum-targeting iridium(III) complex induces immunogenic cell death in melanoma cells and enhances anti-PD-1 immunotherapy by remodeling tumor microenvironment†

Yi Rong,[a] Zhongxian Fan,[b] Zhijie Yu,[a] Li Wei,[b] Han Shen,[a] Huaiyi Huang,[b] Xiaojuan Hao,[a,c] Zizhuo Zhao[d] and Jinquan Wang *[a]

Received 6th June 2023,
Accepted 17th July 2023

DOI: 10.1039/d3qi00841j

rsc.li/frontiers-inorganic

One of the major challenges for immune checkpoint blockades (ICBs) lies in melanoma with limited T cell responses or immunologically "cold" tumors. Inspired by the immunogenicity of immunogenic cell death (ICD) that renders tumor cells sensitive to ICBs, in the present study, an endoplasmic reticulum (ER) targeting iridium(III) metal complex (**IrC**) was investigated as an ICD inducer. It was found that the **IrC**-treated tumor cells showed the hallmarks of ICD, including cell surface exposure of the endoplasmic reticulum protein calreticulin (CRT), secretion of high mobility group box 1 protein (HMGB1), and release of adenosine triphosphate (ATP). The vaccination of syngeneic immunocompetent mice with **IrC**-treated dying cells resulted in anti-tumor immunity with $CD8^+$ T cell response, $Foxp3^+$ T cell depletion, and memory immunity effect. Furthermore, tumor-bearing mice treated with **IrC** + anti-PD-1 combination therapy showed proinflammatory cytokines secretion, increased dendritic cells (DCs) activation, and $CD8^+$ T cell infiltration within the tumor, indicating that the combinatorial therapy reconstructs the tumor microenvironment (TME) and converts an immune "cold" tumor into a "hot" one. This work provides a promising strategy for cancer chemo-immunotherapy.

## Introduction

Melanoma is the most dangerous type of skin cancer with the worst prognosis and the highest mortality rate.[1] The traditional treatments for melanoma include surgical resection, chemotherapy, and radiotherapy, which have limited efficacy and are often accompanied with severe side effects.[2] In recent years, new generation therapeutic drugs such as small molecule kinase targeting inhibitors and ICBs have been developed and contributed to promote the quality of life and survival rates of patients.[3] The ICBs represented by anti-PD-1 antibodies (nivolumab and pembrolizumab) and anti-PD-L1 antibodies (durvalumab and atezolizumab) are approved by the FDA of the United States and led to remarkable survival benefits in melanoma patients.[4] However, adverse side effects and drug resistance are the main barriers for therapeutic effectiveness. In particular, only 20–30% of clinical patients are sensitive to ICBs immunotherapy, which severely limits their clinical use.[5] Advances in knowledge about the pathophysiological mechanisms of melanoma have revealed that the low response rate of melanoma to immunotherapy was due to the host immunosuppressive state.[6] There was a lack of cytotoxic T lymphocytes (CTLs) in the tumor tissue of non-sensitive patients, which showed immunosuppressive tumor microenvironment (TME), so-called the "cold" tumor.[7] Therefore, how to activate the immune system of non-sensitive patients and turn "cold" tumors into "hot" ones by remodeling the TME is the key to improve the therapeutic effect of ICBs on melanoma.

Recent studies suggest that some chemotherapeutic antitumor drugs, such as oxaliplatin,[8] doxorubicin,[9] and cyclophosphamide,[10] can induce ICD of tumor cells, which may trigger

[a]Guangdong Provincial Key Laboratory of Advanced Drug Delivery, School of Bioscience and Biopharmaceutics, Guangdong Pharmaceutical University, Guangzhou, 510006, P. R. China. E-mail: wangjinquan@gdpu.edu.cn
[b]School of Pharmaceutical Science (Shenzhen), Shen Zhen Campus of Sun Yat-Sen University, Shenzhen, 518107, P. R. China
[c]Wenzhou Institute, University of Chinese Academy of Sciences, Wenzhou, Zhejiang 325001, P. R. China
[d]Department of Ultrasound, Sun Yat-Sen Memorial Hospital, Sun Yat-Sen University, Guangzhou, 510275, P. R. China

† Electronic supplementary information (ESI) available. See DOI: https://doi.org/10.1039/d3qi00841j

robust antitumor immune responses.[11] Tumor cells undergoing ICD release damage-associated molecular patterns (DAMPs), which include cell surface exposure of CRT, secretion of ATP, and release of HMGB1.[12] These DAMPs could activate immune system, increase the infiltration of CTLs into tumor tissue, transform "cold" tumor into "hot" one, and thus enhance the efficacy of ICBs for immunotherapy.[13] Growing evidence indicates that the immunomodulatory ability of chemotherapeutic drugs may be more important than their cytotoxicity, and the effect of ICD *in vivo* is independent of the cytotoxicity of chemotherapeutic drugs themselves.[14] Chemotherapeutic drugs with ICD effect can activate the antitumor immunity of the body and enhance the immunotherapeutic effect of ICBs while reducing the toxicity of chemotherapeutic drugs.[15] Therefore, "chemo-immunotherapy" may become the most promising modality for the treatment of melanoma.[16]

The traditional understanding of classical metallic anticancer drugs represented by cisplatin was that it would induce immunosuppression of the body.[17] However, accumulated evidence revealed that some metallic anticancer drugs such as oxaliplatin can evoke ICD and induce systemic anticancer immune-stimulation for tumor prevention.[18] In addition, a large number of metal-based complexes including platinum(IV) complexes,[19–24] ruthenium(II) complexes,[25–28] iridium(III) complexes,[29–34] copper(II) complexes,[35] and gold complexes[36,37] are being tested as potential ICD inducers. Unfortunately, few of these metal-based ICD inducers have entered human clinical trials.[17,38] Up to date, oxaliplatin is the only metal-based anticancer drug known to induce ICD that has been used in the clinic.[39] Therefore, it is necessary to design and screen novel anticancer metal complexes that can act as ICD inducers for immunotherapies of neoplastic disease. Recently, Chao *et al.* reported that an Ir(III) complex (**Ir1**) containing a bis(2-chloroethyl)-azane moiety acted as a potential ICD inducer in non-small cell lung cancer (NSCLC). **Ir1** is the first iridium-based complex that can develop an immunomodulatory response by ICD.[30] However, the synergistic therapy in combination with ICBs has not yet been investigated. Therefore, we propose that the combination of iridium-based ICD inducer and anti-PD-1 therapy may increase the immunogenicity of melanoma and enhance anti-PD-1 immunotherapy by reprograming its "cold" TME.

Fluorination is an important strategy for structure-based medicinal chemistry and comprises a substantial proportion of commercially available drugs such as Efavirenz, Gemcitabine, and others.[40,41] Fluorinated compounds can modulate the physicochemical and pharmacokinetic properties of drugs *via* improving the bioavailability, enhancing the selectivity and binding affinity to cellular targets, and increasing the metabolic stability of drugs.[42,43] However, fluorinated metallic anticancer complex has been seldom reported. Previously, our group have designed and synthesized four novel Ir(III) complexes (Ir1–Ir4). Ir1–Ir3 showed photoinduced catalytic anticancer activity.[44] Interestingly, we recently found that Ir4 (termed **IrC** in this work) coordinated with the trifluoromethyl group showed potent cytotoxicity to cancer cells. Notably, **IrC** was mainly accumulated in the ER and induces ER stress. Inspired by these finding, we evaluate the anticancer efficacy and mechanism of **IrC** as an ICD inducer in the present study.

In this work, we demonstrated that **IrC** could induce ICD through ER stress pathway in melanoma cells. In addition to the ROS generation, **IrC** treatment leads to T cell infiltration, DCs maturation, and proinflammatory cytokines secretion involved with antitumor immunity activation. This promising ICD induction strategy significantly converted tumor cells into an endogenous vaccine and boosted the effects of anti-PD-1 (Scheme 1). These results provide a novel insight into the mechanisms of iridium-based complex induced immunogenicity and establish a strategy to enhance immunotherapy by combining metal-based anticancer agent with ICBs.

## Results and discussion

### The photophysical properties of IrC in solution

The fluorinated tridentate ligand and **IrC** were prepared following our previous reported methods with minor modification (Fig. S1 and S2†).[44] According to the lipo-hydro partition coefficient results, **IrC** exhibited positive log*P* value (+1.45 ± 0.08) which may enhance cell uptake efficiency. **IrC** exhibited strong absorption at 250–270 nm, the luminescence emission maxima of **IrC** was located at 615 nm (Fig. 1A). Upon excitation, **IrC** showed more intense phosphorescence signal ($\lambda_{ex/em}$ = 405/615 nm) in hydrophobic solvent dichloromethane (DCM) than in $H_2O$. In addition, it is found that the emission intensity of **IrC** in the presence of human serum albumin (HSA) was enhanced significantly compared to that measured in $H_2O$ (Fig. 1B). In addition, the stability of **IrC** in FBS was assessed by HPLC, and no changes of **IrC** were observed after being incubated with FBS for 48 h (Fig. S3†). These results demonstrated that the introduction of fluorine atom could enhance the interaction of protein and the hydrophobic microenvironment such that the protein pocket will enhance the phosphorescent intensity of **IrC**.

### IrC induces cytotoxicity, cell apoptosis, ROS and its cellular localization in melanoma cells

We examined the *in vitro* cytotoxic activity of **IrC** against human melanoma A375 cells by MTT assay. As shown in Fig. 2A, **IrC** displayed a high cytotoxicity towards the A375 cancer cells, with the half inhibitory concentrations ($IC_{50}$) values of 4.3 μM and 2.6 μM for 24 h and 48 h, respectively. In addition, CDDP ($IC_{50}$ = 31.2 μM and 16.3 μM for 24 h and 48 h, respectively) was less effective than **IrC** under the same condition, indicating that **IrC** has a better chemotherapeutic profile than cisplatin.

To determine whether **IrC** and CDDP causes cell death by apoptosis, annexin V/PI co-staining assay was carried out. The annexin V positive staining in the cell surface is a hallmark of early-phase apoptosis. In combination with the membrane-

 

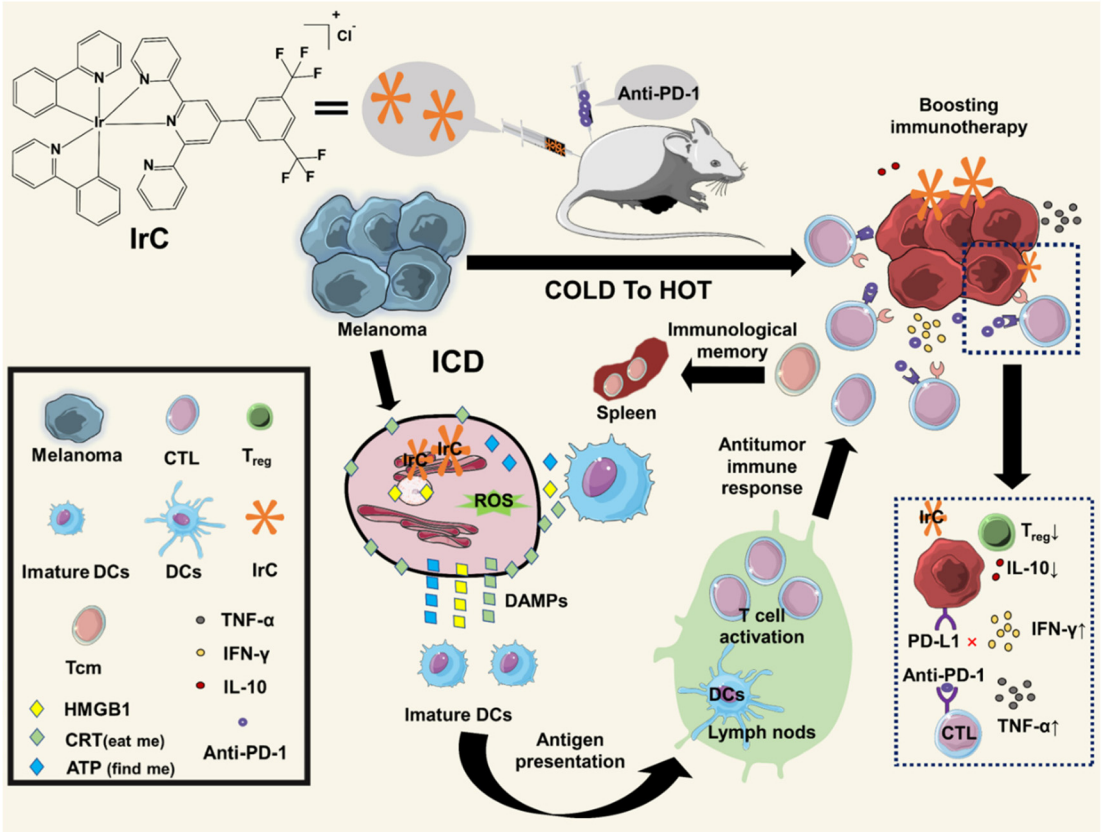


**Scheme 1** Schematic illustration of **IrC**-induced ICD for sensitizing melanoma to PD-1 checkpoint blockade immunotherapy.

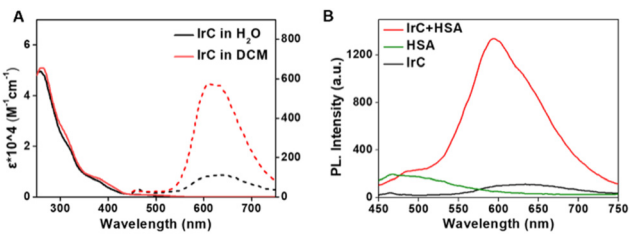


**Fig. 1** Photophysical properties of **IrC** in solution. (A) UV-Vis and phosphorescence spectra of **IrC** (50 μM) in $H_2O$ and DCM. (B) Phosphorescence spectra of **IrC** (50 μM) in the absence and presence of HSA (50 μM) in $H_2O$, $\lambda_{ex}$ = 405 nm.

impermeable DNA stain PI, one can use a flow cytometer to distinguish viable cells and apoptosis cells.[45] The results showed an increased population in the $AV^+PI^-$ and $AV^+PI^+$ regions after being treated with **IrC** or CDDP for 24 h. Due to that cells were treated with the dose at the $IC_{50}$ of **IrC** (4 μM) or CDDP (30 μM), similar apoptotic rates were obtained (Fig. 2B). The results of annexin V/PI co-staining assay suggested that the toxicity of **IrC** and CDDP is attributed to cell apoptosis.

In order to further investigate the mechanism of the cellular toxicity of **IrC**, the intracellular distribution of **IrC** was observed under a confocal laser scanning microscope (CLSM) by colocalization assay with ER-Tracker Green (ERTG), Mito-Tracker Green (MTG), and Lyso-Tracker Green (LTG) probe in A375 cells. The co-stain patterns of **IrC** matched poorly with those of LTG and MTG. Whereas, an excellent superimposition between the signals of **IrC** (red) and ERTG (green) was observed in the overlap images, with a Pearson correlation coefficient of 0.86, indicating that **IrC** selectively localized in the ER (Fig. 2D). In addition, the cellular uptake of **IrC** was quantified by ICP-MS. The results indicated that **IrC** preferentially accumulated in the ER of A375 cells, which is consistent with the results of the colocalization assay (Fig. 2C).

It has been reported that some iridium(III) complexes could induce excessive reactive oxygen species (ROS) in tumor cells, which would lead to apoptosis.[30] Therefore, we investigated whether **IrC** could increase the ROS level in A375 cells using a ROS probe (DCFH-DA). The strong green fluorescence signals were observed in the cells treated with **IrC**, indicating the generation of ROS. On the contrary, the control cells that were incubated with PBS showed no fluorescence. The cells treated with CDDP showed a weak green fluorescence, indicating that CDDP could induce a small amount of ROS in A375 cells (Fig. 2E). In addition, an increase of ROS was detected by flow cytometry after **IrC**-treatment, which is consistent with the results observed by CLSM (Fig. 2F). These data suggested that the toxicity of **IrC** likely results from the intracellular ROS generation.

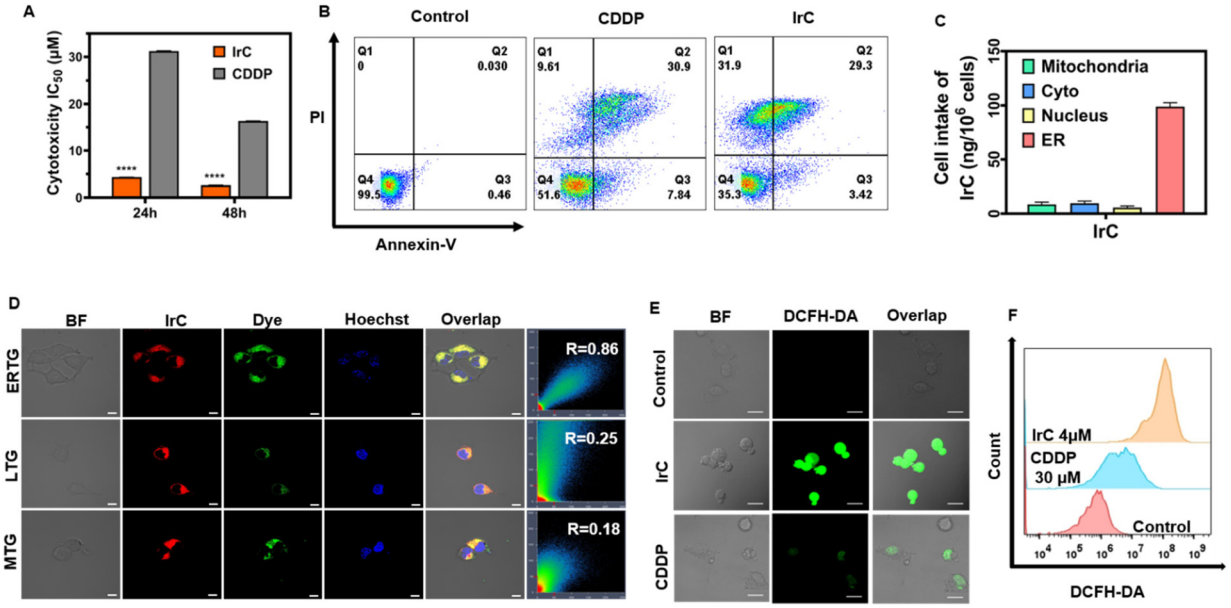


**Fig. 2** **IrC** induces cytotoxicity, cell apoptosis, and ROS, and its cellular localization in A375 melanoma cells. (A) Half inhibitory concentrations ($IC_{50}$) of **IrC** and CDDP in A375 cells. (B) Apoptosis determined by flow cytometry with annexin V/PI co-staining assay. (C) Cellular uptake of **IrC** in the nucleus, lysosomes, mitochondria and ER of A375 cells was quantified by ICP-MS. (D) Co-localization of **IrC** in A375 cells by CLSM. MTG: Mito-Tracker™ Green, ERTG: ER-Tracker™ Green, LTG: Lyso-Tracker™ Green. (E) **IrC** and CDDP induces ROS generation in the A375 cells detected by CLSM. (F) Detection of ROS by flow cytometry. Scale bar: 50 μm.

### IrC induces ICD in melanoma cells through ER stress

The subcellular target determines the initial interaction after the drug was up taken by cells. Due to the fact that **IrC** preferentially accumulated in the ER of the cells, and induced ROS in ER, we wonder if **IrC** could damage the ER and initiate ER stress. Thus, two ER stress related proteins, p-eIF2α and CHOP were examined by western blot. The results showed that p-eIF2α and CHOP were up-regulated after the cells were treated with **IrC**. In contrast, only slight up-regulation of p-eIF2α and CHOP was observed in the CDDP treated cells (Fig. 3A). These data indicated that **IrC** could induce ER stress, which is a critical factor in the signaling cascades leading to ICD. Furthermore, the hallmarks of ICD, namely DAMPs, including CRT, HMGB1 and ATP were investigated. The extracellular HMGB1 in the medium supernatant was detected by western blot. The release of HMGB1 from A375 cells treated with **IrC** (4 μM) was increased greatly, about 5 times as high as that in the CDDP treated cells (Fig. 3B). The surface exposure of CRT was detected by immunofluorescence and observed by CLSM. CRT on the cell surface of A375 cells was identified by green fluorescence after being treated with **IrC** (4 μM) for 24 h. However, only very weak fluorescence signal was detected in CDDP-treated A375 cells, which suggested the failure of CDDP to induce ICD in melanoma cells (Fig. 3C). In addition, an earlier time point of 12 h was performed to quantify the CRT exposure by flow cytometry after being treated with **IrC** (4 μM) or CDDP (30 μM). The **IrC** group (24.00%) showed significant increase of CRT positive cells compared to the CDDP group (6.49%) and the control group (1.05%), which is in accordance

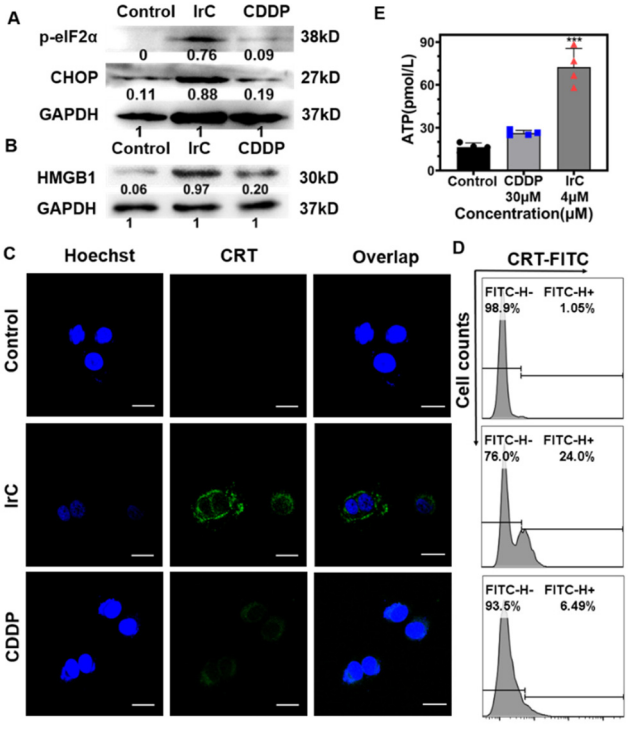


**Fig. 3** Hallmarks of ER stress and ICD in A375 cells treated with **IrC** (4 μM) or CDDP (30 μM). (A) The expression of p-eIF2α and CHOP. (B) The extracellular HMGB1 in the medium supernatant was detected by western blot. (C) CLSM images of CRT on cell surface. Scale bars: 50 μm. (D) The quantitative evaluation of CRT exposure was detected by flow cytometry. (E) The extracellular release of ATP after **IrC** and CDDP treatment. *** = $P < 0.001$, compared with the control group.

with the results obtained by CLSM (Fig. 3D). ATP is an important molecule that is secreted by cells during the process of ICD.[46] Thus, the extracellular release of ATP from A375 cells was measured by a commercial ELISA detection kit. The ATP secretion from A375 cells after being treated with **IrC** (4 μM) was 4.6 times as high as that of the control cells. In comparison, no significant difference of ATP secretion was observed between CDDP (30 μM) treated cells and control cells (Fig. 3E). To approximate the strength of the immune response of **IrC**, we compared and quantified the immunogenic cell death-related hallmarks to a known ICD inducer, oxaliplatin. The A375 cells were treated with **IrC** (6 μM) or oxaliplatin (70 μM) for 12 hours at the $IC_{50}$, respectively (Fig. S4A†). The ATP secretion of **IrC** group was 3.5 times as high as that of the control group, and the oxaliplatin group was 3.7 times as high as that of the control group (Fig. S4B†). Additionally, the quantitative analysis of western blot showed that the release of HMGB1 increased significantly in the **IrC** group (9.2 times) and oxaliplatin group (9.4 times) compared to the control group (Fig. S4C†). In comparison, the percentage of CRT positive cells in the **IrC** group (26.2%) and oxaliplatin group (24.2%) showed significant increase compared the control group (0.87%), which is in accordance with the results obtained by CLSM (Fig. S4D and E†). Collectively, the results of the ATP secretion, HMGB1 release, and CRT translocation demonstrated that **IrC** could induce effective ICD in the A375 cells *in vitro*. Notably, **IrC** and oxaliplatin have a similar capability to induce ICD. Accumulating evidence revealed that these signaling molecules known as DAMPs could potentiate systemic antitumor immune responses.

For example, ATP released by tumor cells acts as a "find me" signal, which enhances the tumor recognition ability of immune cells.[47] CRT, as the "eat me" signal, can enhance antitumor immunity,[48] and HMGB1, as a binder to immune cells, can promote the recovery of immune surveillance.[49] However, these assays to examine ICD related DAMPs can only identify **IrC** as an ICD inducer *in vitro*. To further explore the possibility that **IrC** promotes ICD in mice models, we also applied the same set of experiments to the murine origin melanoma cells B16-F10 (Fig. S5–S7†). Encouragingly, the data suggested that **IrC** induced ICD in B16-F10 cells with similar results to A375 cells. Therefore, we next performed *in vivo* experiments to examine the immune activation effect of **IrC** using B16-F10 cells.

### IrC induces ICD in a syngeneic mouse model

The gold standard for evaluating the ability of a chemical agent as a bona fide ICD inducer requires vaccination experiment with an immunocompetent mouse model.[17] Therefore, we evaluated the ICD effect of **IrC** in a syngeneic mouse model by vaccination experiment using immunocompetent C57BL/6 mice.[30] The mice of **IrC** group and CDDP group were injected with the dying B16-F10 tumor cells treated with **IrC** or CDDP, separately. The mice of the control group were injected with the B16-F10 cells treated with the solvent. A week later, all the mice from these three groups were rechallenged by injecting the same type of live tumor cells (Fig. 4A). Tumor volume was monitored for 15 days, as shown in Fig. 4B–D. Vaccination with cells treated with **IrC** showed pronounced tumor rejection in immunized mice of **IrC** group at the end of vaccination experiment on the day 15. However, no statistical difference of tumor inhibition was observed between CDDP and control group. Histological examination (H&E) of the tumors that were collected from the mice confirmed these results. Tumor tissues from **IrC** group displayed severe alterations, including nucleus fragmentation and breakdown of cytoplasmic structure, which indicated necrosis or apoptosis of the tumor cells. However, slightly damage was observed in the tumors of CDDP group (Fig. 4E).

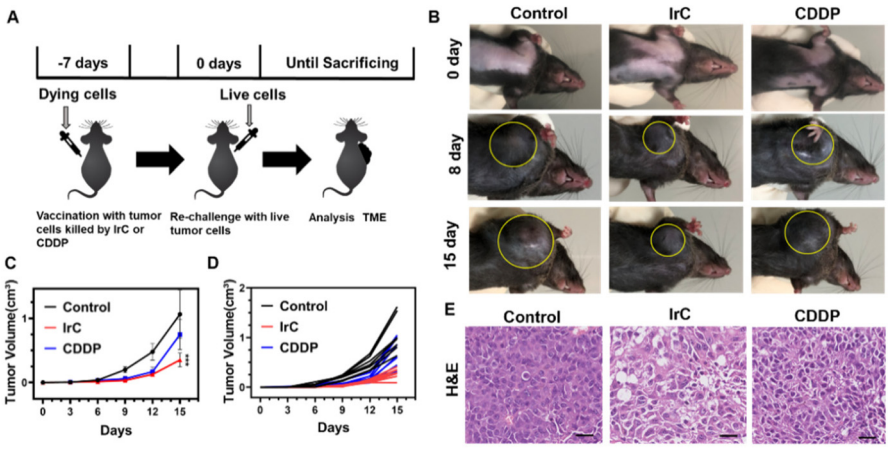


**Fig. 4** B16-F10 melanoma tumor vaccine experiment in C57BL/6 mice. (A) Schematic of the ICD vaccine experiment. (B) Representative photographs in vaccinated mice following different treatments. (C) Individual tumor growth curves of the rechallenged mice with different vaccination. (D) Average tumor growth curves of the rechallenged mice with different vaccination. (E) H&E staining results of tumor slices collected from mice in each group. *** = $P < 0.001$, compared with the control group.

In addition, the body weight of mice in these three groups showed no significant difference throughout the experiments (Fig. S8†). The H&E staining of the main organs (heart, liver, spleen, lungs, kidneys) showed no significant histological damage in all treated groups (Fig. S9†). Taken together, these results demonstrate that **IrC** could promote ICD induction in syngeneic mouse model *in vivo*.

### ICD effect induced by IrC could induce systemic immune stimulation

Encouraged by the robust local antitumor immune responses in the vaccination experiment, we next investigated if the ICD effect induced by **IrC** could induce systemic immune stimulation. The tumor-draining lymph nodes (TDLNs) and tumors were retrieved from the mice with vaccination experiment and the immune cells were isolated and analyzed by flow cytometry.

As illustrated in the Fig. 5A and B, the **IrC** group (29.1%) showed significant increase of the matured DCs ($CD80^+CD86^+$) in TDLNs compared to the CDDP group (12.0%) and the control group (17.6%) with statistical difference. These results suggested that **IrC** could promote DCs maturation in the lymph nodes, which play a key role in initiating and regulating the innate and adaptive immunity. In addition, the presence of $CD8^+$ T cells, termed as cytotoxic T lymphocytes (CTLs) in the tumor tissue of the mice were quantified by flow cytometry. The proportion of $CD8^+$ T cells in the **IrC** group (25.8%) was much higher than that in the CDDP group (17.2%) and the control group (12.8%) (Fig. 5C and D). Furthermore, immunofluorescence analysis showed the most enrichment of $CD8^+$ T cells in the tumor tissue of **IrC** group (Fig. 5E and F), indicating the effective infiltration of CTLs into the tumors. The immunosuppressive cells, $Foxp3^+$ T cells in the tumor tissue of the mice were also determined. As shown in Fig. 5G and H, the number of $Foxp3^+$ T cells in the **IrC** group was much less than that of CDDP group and control group. To further determine the systemic immune response, we evaluated the cellular cytokines in the serum of the mice in different groups. The levels of proinflammatory cytokines (TNF-α and IFN-γ) in serum of **IrC** group were significantly higher than that of CDDP group and control group (Fig. 5I and J). The concentration of anti-inflammatory cytokine IL-10 of **IrC** group was lower than that of CDDP group and control group (Fig. 5K). Collectively, these data demonstrated that the ICD effect induced by **IrC** could induce systemic immune stimulation by regulating the immune cells and immune molecules.

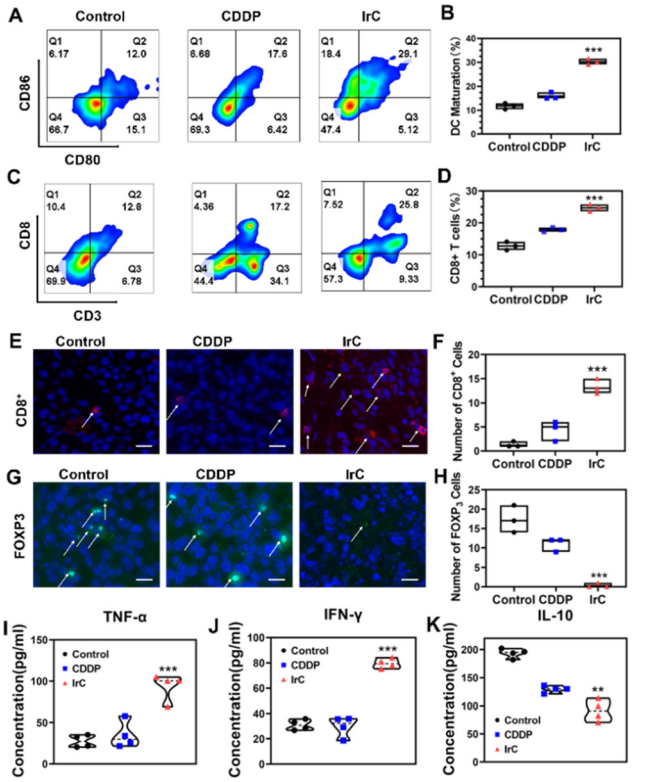


**Fig. 5** The ICD effect induced by **IrC** induced systemic immune stimulation in the mice in the vaccine experiment. (A) The presence and the quantification (B) of mature DC induced by ICD effect in tumor-draining lymph nodes of the mice. (C) The presence and the quantification (D) of $CD8^+$ T cells in the tumors of the mice. (E) Immunofluorescence images (red: $CD8^+$; blue: Hoechst 33324) and the quantification analysis (F) of the number of $CD8^+$ T cells. (G) Immunofluorescence images (green: $Foxp3^+$; blue: Hoechst 33324) and the quantification analysis (H) of the number of $Foxp3^+$ cells. Concentration of the TNF-α (I), IFN-γ (J), and IL-10 (K) in the serum of the mice in different groups. Data from 3 biologically independent samples for B, D, F, and H. Scale bars: 100 μm. Data from 4 biologically independent samples for H, I, and J. ** = $p < 0.01$; *** = $p < 0.001$, compared with the control group.

### IrC elicits antitumor immunological memory

In general, the central memory T cells ($T_{CM}$) provide immune protections after antigen stimulation, whereas the effector memory T cells ($T_{EM}$) induce immediate protections by producing proinflammatory cytokines, such as IFN-γ.[50] In order to evaluate whether the **IrC**-induced systemic immune responses were durable, we further analyzed the $T_{CM}$ and $T_{EM}$ in the PBMC and spleen from the mice at the end of vaccination experiment. The antitumor capacity of the immune memory cells was evaluated by co-culturing the PBMC with B16-F10 cells *in vitro*. The cytotoxic effect of PBMC on B16-F10 cells was determined by calcein acetoxymethyl (Calcein-AM) staining assay. The intracellular nonfluorescent Calcein-AM can be converted into the intensely green fluorescent calcein by the esterase in living cells, so the cell viability could be quantified by the fluorescence intensity of the target cells.[51] The PBMC from the **IrC** group exhibited much higher relative cytotoxicity against tumor cells than that of CDDP group and the control group (Fig. 6A). The flow cytometric analysis indicated that the proportions of $T_{EM}$ and $T_{CM}$ in the PBMC of **IrC** group showed markedly increase compared with CDDP group and control group (Fig. 6B and C). In addition, the percentages of $T_{EM}$ and $T_{CM}$ cells in the spleens showed similar results as that in the PBMC (Fig. S10†). These data demonstrated the immune

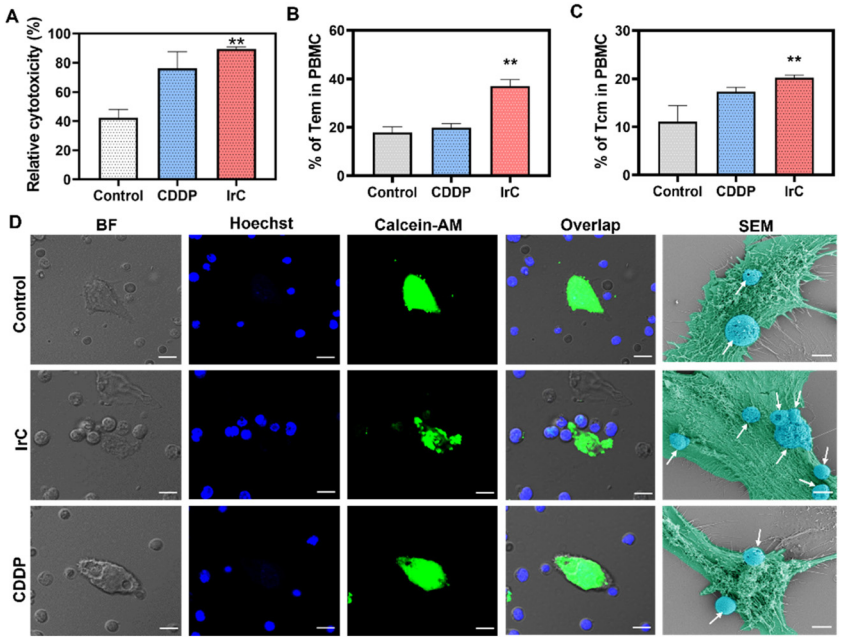


**Fig. 6** **IrC** triggered immunological memory in the vaccinated C57BL/6 mice. (A) The cytotoxic effect of PBMC on B16-F10 cells was quantified by Calcein-AM staining assay. (B) Proportions of $T_{EM}$ cells ($CD3^+CD8^+CD44^+CD62L^-$) in the PBMC. (C) Proportions of $T_{CM}$ cells ($CD3^+CD8^+CD44^+CD62L^+$) in the PBMC. (D) PBMC (Hoechst) co-culture with B16-F10 cells (Calcein-AM) observed by CLSM (scale bar = 50 μm) and SEM (scale bar = 5 μm). * = $p < 0.05$; ** = $p < 0.01$; compared with the control group.

memory effect in the mice of **IrC** group. The B16-F10 cells were stained by Calcein-AM and PBMC were stained by Hoechst 33324, and observed under CLSM. After being co-cultured for 4 h, the number of PBMC around the tumor cells in the **IrC** group showed significant increase. However, only few numbers of PBMC were observed around the target cells in the CDDP group and control group. In addition, scanning electron microscopy (SEM) was used to observe the cell interactions, most PBMC tightly bound to the tumor cells in the **IrC** group, which is in accordance with the results obtained by CLSM (Fig. 6D). These results of the co-culture experiments not only support the vaccination experiment, but also confirm that the memory immunity effect induced by **IrC** is involved in antitumor immune responses.

### IrC enhances anti-PD-1 immunotherapy *in vivo*

Recent studies revealed that some tumors show striking features of CTLs absence, which are known as immunologically "cold", and do not respond to ICBs.[52] However, our results indicated that **IrC** may convert the immunosuppressive "cold" tumors into immune-responsive "hot" ones and enhance tumor response to PD-1 checkpoint blockade immunotherapy. Therefore, we further examined whether **IrC** could boost the anti-tumor immunity of PD-1 inhibitors using a poorly immunogenic B16-F10 melanoma model *in vivo*. CDDP was selected as a control agent because it does not have ICD-inducing ability in B16-F10 melanoma. The results showed that the CDDP treatment alone only slightly suppressed tumor growth. **IrC** or PD-1 treatment alone, and CDDP + PD-1 groups, induced a statistical tumor growth delay *versus* control group. These three groups showed similar inhibition of tumor growth. Moreover, compared with the control group, **IrC** + PD-1 group showed the most significant tumor inhibitory effect during the 12 days observation period (Fig. 7A and B). Histological examination of the tumors slices from different groups confirmed these results. The tumor tissues of the CDDP group were partially damaged. In addition, the tumor tissues of the **IrC** or PD-1 treatment alone, and CDDP + PD-1 groups showed moderated damage. Moreover, a large proportion of the tumor tissues was noted to have displayed shrunken cells without nucleus in the **IrC** + PD-1 group, which reflects severe necrosis or apoptosis of the tumor cells (Fig. 7D). Furthermore, in corresponding to H&E results, the most amount of green fluorescence signals of the TUNEL assay were observed in the **IrC** + PD-1 group, indicating the highest proportion of apoptotic cells in the tumor tissues (Fig. 7E). In addition, signs of toxicity, such as emaciation and decreased body weight were observed in the mice of CDDP and CDDP + PD-1 groups (Fig. 7C). Additionally, histopathology examination showed proximal tubular cell degeneration and kidney glomerulus atrophy in these two groups (Fig. 7F), which was inconsistent with the previous report.[53] On the contrary, no body weight loss and other severe side effects were observed in the mice of **IrC**, PD-1, and **IrC** + PD-1 groups. The histological analysis of the other main organs (liver, heart, spleen and lungs) showed no significant pathological lesion in all treated groups (Fig. S11†). In addition, the hemolytic analysis

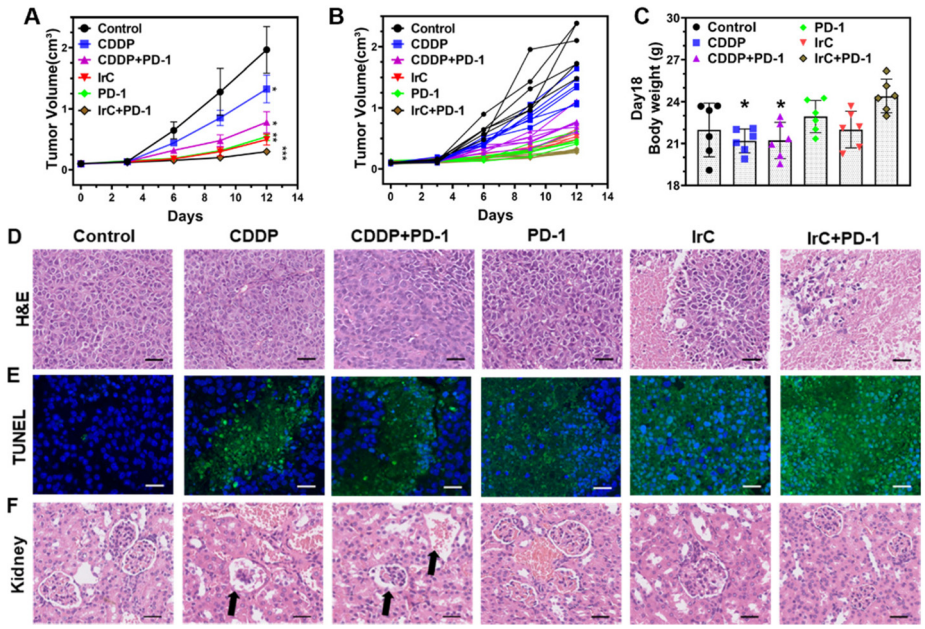


**Fig. 7** The therapeutic effect on B16-F10 tumor bearing mouse model with different treatment strategies. (A) Individual tumor growth curves of the mice. (B) Average tumor growth curves of the mice. (C) Average body weight of the mice in each group after removing the tumor. (D) H&E staining results of tumor slices collected from the mice. (E) TUNEL staining (green: TUNEL positive; blue: DAPI) results of tumor slices collected from mice. (F) H&E staining results of kidney slices collected from the mice in each group. Scale bars: 100 μm. Data represent mean ± SEM ($n$ = 6), * = $p$ < 0.05, ** = $p$ < 0.01; *** = $p$ < 0.001, compared with the control group.

showed that the incubation of red blood cells (RBCs) with **IrC** did not cause any hemolysis at the treatment concentration (Fig. S12†), confirming the good hemocompatibility of the **IrC**. Collectively, **IrC** could enhance the anti-tumor immunity of PD-1 in B16-F10 tumor-bearing C57BL/6 mice and possesses relatively high biosafety *in vivo*.

## IrC reconstructs the TME immune phenotype of "cold" tumor into "hot" one

To further confirm if **IrC** could remodeling the TME of the poorly immunogenic melanoma model, we exanimated the CTLs ($CD8^+$ T cells) and the immunosuppressive cells ($Foxp3^+$

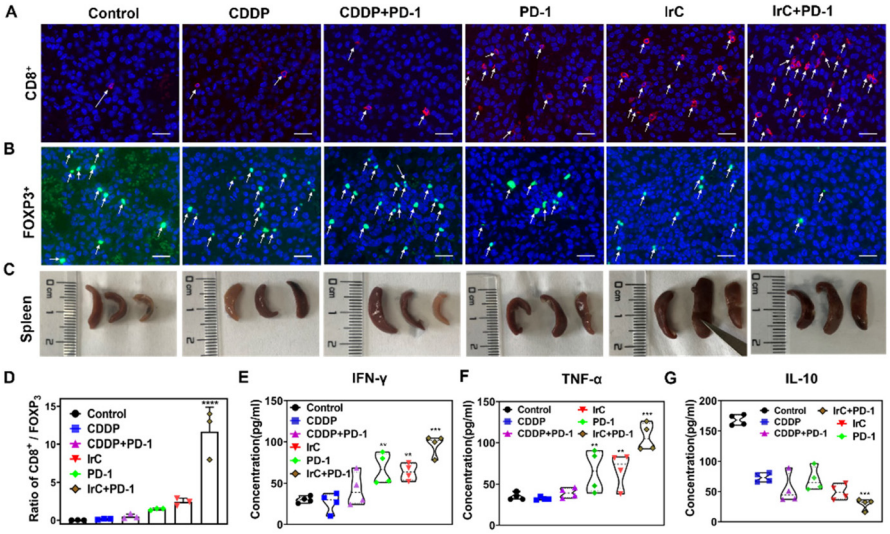


**Fig. 8** Assessment of the immune status of the tumor-bearing mice with different treatment. (A) Immunofluorescence images (red: $CD8^+$; blue: DAPI) of $CD8^+$ T cells in the tumor of the mice in each group. (B) Immunofluorescence images (green: $Foxp3^+$; blue: DAPI) of $Foxp3^+$ cells in the tumor of the mice in each group. (C) Photographs of the spleens retrieved from the mice in each group. (D) The proportion of $CD8^+/Foxp3^+$ in the tumor tissues of the mice in each group. Concentration of the TNF-α (E), IFN-γ (F), and IL-10 (G) in the serum of the mice in different group. Data from 4 biologically independent samples. Scale bars: 100 μm. ** = $p$ < 0.01; *** = $p$ < 0.001, compared with the control group.

 

T cells) in the tumor tissues of the mice in different groups. As shown in Fig. 8A, there were almost no $CD8^+$ expressing CTLs infiltrated in the tumors of the control group, which was a symbol of "cold" tumors. However, the red fluorescence signals of $CD8^+$ T cells were observed the most in the **IrC** + PD-1 group, indicating the highest level of $CD8^+$ positive cells infiltration in the tumor tissues and the ability of **IrC** to enhance the local immune responses. Whereas, few $CD8^+$ T cells were observed in the tumors of CDDP and CDDP + PD-1 groups, possibly due to the insufficient ICD-inducing ability of CDDP. The abundance of $Foxp3^+$ T cells represent the suppression of immune responses in the tumor and the $CD8^+$/$Foxp3^+$ ratio is a critical parameter to evaluate the antitumor immune responses.[52] As expected, only few green fluorescence $Foxp3^+$ signals were observed in the tumor tissues from the **IrC** + PD-1 group (Fig. 8B). Furthermore, the **IrC** + PD-1 group showed the highest proportion of $CD8^+$/$Foxp3^+$ in all the treated groups (Fig. 8D). These data indicated that **IrC** mediated ICD combined with PD-1 therapy significantly reduced tumor-associated immunosuppression. Notably, the B16-F10 tumor bearing mice of the **IrC** treated group showed swollen spleen, indicating that the **IrC**-induced tumor ablation *in vivo* is a proinflammatory process, which was inconsistent with the recent report.[54] Interestingly, the **IrC** + PD-1 treatment could make the swollen spleen of the mice return to normal level after treatment, indicating that combination treatment group showed better body tolerance, which is important for the safe use in the clinic (Fig. 8C). The ELISA assay results showed that the contents of proinflammatory cytokines IFN- γ and TNF-α in the serum were substantially increased in the mice of **IrC** or PD-1 treatment alone groups. Moreover, the **IrC** + PD-1 treatment group showed the most significant increase compared with the control group (Fig. 8E and F). In addition, the content of immunosuppressive cytokine IL-10 of all the treatment groups was lower than that of control group (Fig. 8G). These results demonstrated that the immune system of **IrC** + PD-1 group is effectively activated, and the **IrC** + PD-1 treatment could turn the "cold" tumor into a "hot" one due to the induction of inflamed microenvironment.

# Conclusions

We successfully demonstrated that **IrC** could induce ICD in melanoma cells through ER stress pathway. The **IrC** induced-ICD effect not only rejected tumor rechallenge by B16-F10 melanoma but also generated antitumor memory immune response. Furthermore, the **IrC** and anti-PD-1 combination therapy efficiently remodeled the tumor-immunosuppressive microenvironment, including more $CD8^+$ T cell infiltration, DCs maturation, and the secretion of antitumor associated cytokines, therefore, turning immunosuppressive "cold" tumor to immune-responsive "hot" one and potentiating the anti-tumor effect of PD-1 inhibitors. In addition, **IrC** showed no adverse effects in the *in vivo* experiment. This study will provide a rationale for combining metal drug chemotherapy with immunotherapy in clinics.

# Experimental section

### Materials and general instrumentation

Iridium complex (**IrC**) $[Ir(ppy)_2(L)]Cl$, where ppy = 2-phenylpyridine, L = 4′-(3,5-bis(trifluoromethyl)phenyl)-2,2′:6′,2″-terpyridine was prepared and characterized according to our previous report.[44] All reagents and solvents from commercial sources were of analytical grade unless otherwise noted. Iridium(III) chloride trihydrate was purchased from Kunming Institute of Precious Metal. Cisplatin (CDDP), oxaliplatin, 3-(4,5-dimethylthiazol-2-yl)-2,5-diphenyltetrazolium bromide (MTT), Hoechst 33342 were purchased from Sigma-Aldrich (USA). Mitotracker™ Green, Lyso-Tracker™ Green, ER-Tracker™ Green, were purchased from Thermo (USA). Reactive oxygen species assay kit and calcein acetoxymethyl (Calcein-AM) cell viability assay kit were purchased from Beyotime (China). Calreticulin (D3E6) XP® Rabbit mAb (Alexa Fluor® 488 Conjugate) was purchased from CST (USA). ENLITEN® ATP assay system bioluminescence detection kit was purchased from Promega (USA). IFN-γ, TNF-α, and IL-10 ELISA kit were purchased from Multi-sciences (China). αPD-1 antibody (RMP1–14) was purchased from Bioxcell (USA). TUNEL staining kit was purchased from Biossci (USA). Mouse peripheral blood lymphocyte (PMBC) isolation kit, mouse tumor infiltrating lymphocyte isolation kit and heparin sodium salt were purchased from Solarbio (China). The inductively coupled plasma mass spectrometry (ICP-MS) experiments were carried out on an Agilent 7700x instrument (Thermo Elemental Co., Ltd).

### Characterization of UV-Vis spectroscopy, phosphorescence spectroscopy, and log $P_{o/w}$ measurement

The UV-Vis spectra of **IrC** (50 μM) were obtained at room temperature from 750 to 250 nm with a Yoke T3202S UV-Vis spectrophotometer. The phosphorescence emission measurements of **IrC** (50 μM) in diverse solvents and human serum albumin (HSA) (50 μM) were obtained by a Techcomp FL970 fluorescence spectrophotometer. $\log P_{o/w}$ measurement was performed as followed, **IrC** was added to pre-saturated water and pre-saturated *n*-octanol solution with the final concentration of **IrC** was 100 μM, then the mixture was shaken for 24 h at room temperature. The absorbance of the oil/water phase in acetonitrile solution was measured by a UV-Vis spectrophotometer after stationary. The partition coefficient of **IrC** was calculated from the equation $\log P_{o/w} = \log(C_o/C_w)$, where $C_o/C_w$ represents the concentration of the **IrC** in the octanol/water phase.

### Stability in FBS

The stability test of **IrC** in fetal bovine serum (FBS) was performed as previously described.[30] **IrC** (10 μL, 10 μM, from stock solution 1 mM in DMSO) and diazepam (10 μL, 10 μM, internal reference) were added to FBS (980 μL) to total volume

of 1000 μL. The solution was shaken (~300 rpm) and incubated for 0 or 48 hours at 37 °C respectively. After that, the samples were added 2 mL of acetonitrile, then the mixture was centrifuged (×1000*g*) for 45 min at 4 °C. The supernatants were collected and solvent was evaporated. Then the residue was suspended in 200 μL of ethanol and was filtered. The samples were analyzed by HPLC-UV with a C18 reverse phase column.

### Cell lines and cell culture

A375 human melanoma cells and B16-F10 mouse melanoma cells were obtained from the Shanghai Cell Institute (Cell Bank, Sinica Academia Shanghai, China). These two cell lines were confirmed based on DNA detection techniques by detecting of short tandem repeats (STRs). Cells were cultured in DMEM supplemented with 10% fetal bovine serum and penicillin (100 U $mL^{-1}$)/streptomycin (50 U $mL^{-1}$). Cells were used when they reached logarithmic growth phase.

### Cellular localization and distribution

Melanoma cells were cultured in a 35 $mm^2$ glass-bottom dishes (Corning) and incubated with **IrC** (4 μM) for 24 h. A mitochondria-specific green fluorescent probe Mito-Tracker Green (MTG, 5 μg $mL^{-1}$), or a lysosome-specific green fluorescent probe Lyso-Traker Green (LTG, 5 μg $mL^{-1}$), or an endoplasmic reticulum-specific green fluorescent probe ER-Traker Green (ERTG, 5 μg $mL^{-1}$) and nuclei stain probe Hoechst 33342 (10 μg $mL^{-1}$) were then added to the dishes and incubated for 30 min in the dark. The cells were then washed three times with PBS before the samples were observed under a confocal laser scanning microscope (CLSM, Carl Zeiss 880, Germany). ER-Tracker Green ($\lambda_{ex}$ = 488 nm, $\lambda_{em}$ = 504–511 nm), Lyso-Traker Green ($\lambda_{ex}$ = 488 nm, $\lambda_{em}$ = 510–540 nm), Mito-Tracker Green ($\lambda_{ex}$ = 488 nm, $\lambda_{em}$ = 510–540 nm) and Hoechst 33342 ($\lambda_{ex}$ = 405 nm, $\lambda_{em}$ = 410–450 nm).

Inductively coupled plasma mass spectrometry (ICP-MS) was employed to quantify the cellular uptake of **IrC**, as described in our previous report.[51] A375 cells were incubated with **IrC** (4 μM) for 24 h at 37 °C. After incubation, the whole cell, the mitochondria, endoplasmic reticulum, nuclear and cytoplasm fractions were obtained separately using mitochondrial, endoplasmic reticulum, nuclear and cytoplasm isolation kits respectively. The extractions were subsequently digested by 60% $HNO_3$ for 24 h and analyzed by ICP-MS. The data were reported as the mean ± standard deviation ($n$ = 3) and the results were reported based on the cell number.

### The cytotoxicity and apoptosis assay

MTT assay was employed to measure the cytotoxicity of **IrC** and CDDP on melanoma cells. Briefly, exponentially grown A375 cells were seeded into 96-well culture plates at a density of $1 \times 10^4$ cells per well and incubated at 37 °C for 24 h. Then cells were treated with a range of concentrations of **IrC** or CDDP and incubated for 24 h or 48 h. The half-maximal inhibitory concentration ($IC_{50}$) values were determined by a series of the inhibition rate evaluated by the MTT assay as described in our previous report.[55]

Annexin V/PI co-staining assay was performed by flow cytometry according to the manufacturer's protocol.[30] Briefly, cells were seeded in six-well culture plates and incubated with **IrC** (4 μM) or CDDP (30 μM) for 24 h at 37 °C in a 5% $CO_2$ incubator. After treatment, the cells were trypsinized, washed twice with cold PBS, and resuspended in 100 μL of 1× binding buffer (50 mM HEPES/NaOH, pH 7.4, 700 mM NaCl, 12.5 mM $CaCl_2$). Then 5 μL of annexin V-FITC and 1 μL of PI were added to the cell suspension. After incubation for 15 min at room temperature, another 400 μL of binding buffer was added. Then the stained samples were examined using the flow cytometer.

### Intracellular reactive oxygen species (ROS) measurement

Accumulation of ROS was detected using the DCFH-DA probe according to our previously report.[55] The cells were treated with **IrC** (4 μM) or CDDP (30 μM) for 24 h. Then cells were incubated in 10 μM DCFH-DA for 30 min and washed three times with PBS to remove DCFH-DA. The cells were trypsinized, washed twice with cold PBS, then the samples were quantified by flow cytometry. In addition, the cells were seeded in a 35 $mm^2$ glass-bottom dishes for assessment by CLSM.

### ER stress, cell surface CRT, extracellular HMGB1 and ATP

Western blot was performed to detect the ER stress relative protein phospho-eIF-2α (p-eIF2α, 38 kDa), C/EBP homologous protein (CHOP, 27 kDa), and the ICD hallmark HMGB1 (30 kDa). Briefly, melanoma cells were treated with **IrC** (4 μM) or CDDP (30 μM) for 24 h. Then the cells were collected and washed twice with ice-cold PBS and lysed in RIPA buffer to extract the total cellular proteins for detecting p-eIF2α and CHOP. In addition, the cell culture supernatants were collected and freeze-dried for detecting extracellular HMGB1. The routine western blot procedure was performed as described in our previous report.[56] The antibody HMGB1 (ab79823) was obtained from Abcam (Cambridge, United Kingdom). CHOP (#35744), p-eIF2α (#11279), GAPDH (#41549), and secondary antibody (#13012) were obtained from SAB (USA).

Immunofluorescence was performed to detect the cell surface CRT. Melanoma cells were seeded in a 35 $mm^2$ glass-bottom dishes and treated with **IrC** (4 μM) or CDDP (30 μM) for 24 h. Then the cells were incubated with Calreticulin (D3E6) XP® Rabbit mAb (Alexa Fluor® 488 Conjugate) according to the manufacturer's protocol. After being washed with PBS, the Hoechst 33342 was added and incubated for 15 min. After washing with PBS again, the samples were observed under the CLSM. The excitation wavelength was 488 nm, the emission wavelength was 520 ± 20 nm.

The quantitative evaluation of CRT exposure was detected by flow cytometry. Melanoma cells were treated with **IrC** (4 μM) or CDDP (30 μM) for 12 h. After the incubation, the cells were trypsinized, and washed twice with cold PBS. Then the cells were collected, fixed, and incubated with Calreticulin (D3E6) XP® Rabbit mAb (Alexa Fluor® 488 Conjugate) according to the manufacturer's protocol.[30] Then the stained samples were

 

examined using the flow cytometer, and the binned populations were expressed as % of total cells.

The extracellular ATP was quantified using an ATP detection kit (ENLITEN®, Promega). Melanoma cells were treated as describe above, then the cell supernatants were transferred to the non-transparent bottomed white-walled 96-well plates. The chemiluminescence derived from ATP was measured and calculated on a multifunction full wavelength scanner (Thermo, USA).

### Animal models and therapeutic protocols

Syngeneic C57BL/6 male mice aged 5 weeks were purchased and bred in the experimental animal center, Guangdong Pharmaceutical University (GDPU). All experimental protocols received prior approval from the GDPU Animal Care and Use Committee (approval no.: gdpuspf 2017460-3). All surgical procedures were performed under sterile condition using anesthesia.

For *in vivo* vaccination experiment, the mice were randomly divided into three groups ($n$ = 7), which were named as **IrC** group, CDDP group, and control group. B16-F10 cells were treated *in vitro* with, **IrC** (5 μM), CDDP (50 μM) and the solvent separately for 24 h. Then the treated cells were rinsed in PBS and injected subcutaneously into the left flank of the mice in each group. One week later, mice were re-challenged in the right flanks with live B16-F10 cells ($2 \times 10^6$ cells per 100 μL, sterile PBS/Matrigel, 1 : 1, v : v). Tumor volume ($V$) was measured every 3 days and calculated as $V$ = (length × width$^2$)/2.

For systemic therapy experiments, C57BL/6 male mice were injected in the right flank with B16-F10 ($2 \times 10^6$ cells per 100 μL, sterile PBS/Matrigel, 1 : 1, v : v) to establish a xenograft model. The mice with well grown tumors were randomly divided into six groups ($n$ = 6): control group (PBS), CDDP group (6 mg kg$^{-1}$), **IrC** group (5 mg kg$^{-1}$), PD-1 group (10 mg kg$^{-1}$), CDDP + PD-1 group (CDDP, 6 mg kg$^{-1}$ + PD-1, 10 mg kg$^{-1}$), **IrC** + PD-1 group (**IrC**, 5 mg kg$^{-1}$, + PD-1, 10 mg kg$^{-1}$). Mice then received intraperitoneal injections of the corresponding drugs every three days for 4 times, and the PD-1 antibody was injected 24 hours later after the chemotherapy drugs were administered. Tumor volume ($V$) was measured every 3 days.

### Hemolysis assay

The blood (1 mL) was collected from healthy C57BL/6 mice under anesthesia. Then the sample was washed twice with 4 mL normal saline and centrifuged (600$g$, 5 min). RBC deposit was obtained when the supernatant was colorless and transparent. Then the RBC deposit was diluted with normal saline. Next, various concentrations of **IrC** (5, 10, and 20 μM) were added into the RBC suspension. Distilled water and normal saline were used as positive control and negative control, respectively. The samples were incubated in a 37 °C water bath, and observed 2 h later.

### Hematoxylin–eosin (H&E) and immunofluorescence (IF) staining

The tumors and major organs (including kidney, heart, lung, liver, and spleen) from the different groups were collected after the mice were sacrificed. Parts of the tumors and organs were embedded in paraffin and sliced into 6 μm sections. For the morphological analysis, tumors and major organs sections were stained with H&E by standard procedures including deparaffinization and rehydration (xylene, alcohol, water). For immunofluorescence assay, the sections of tumor were stained with anti-CD8-FITC (ab217344), anti-Foxp3-FITC (ab215206) antibodies (Cambridge, United Kingdom), and images were analyzed by Zeiss Zen (bule edition) software.

### Flow cytometric (FACS) analysis and ELISA assays

DCs maturation and T lymphocyte infiltration were assessed by FACS analysis. Distant tumors and tumor draining lymph nodes of the mice in the *in vivo* vaccination experiment were harvested and digested into single cell suspensions as previously described.[57] Lymphocytes were isolated with a lymphocyte isolation kit. The single-cell suspension was stained with antibodies for CD8$^+$ cytotoxic T cells (anti-mouse CD8-FITC, anti-mouse CD3-PerCP-Cy5.5) and for DC cells (CD86-PE – Cyanine7, anti-mouse CD80-FITC). All samples were analyzed with a flow cytometer and FlowJo software.

The quantification of cytokines TNF-α, IFN-γ, interleukin-10 (IL-10) in mice serum was performed by means of enzyme-linked immunosorbent assay (ELISA), according to the manufacturer's instructions.

### Analysis of memory T cells and their cytotoxicity on B16-F10 cells

For analysis of memory T cells, the spleens of the mice of different treatment groups were collected and the single-cell suspensions were prepared as previously described.[52] In addition, the peripheral blood mononuclear cell (PBMC) of the mice of different groups were collected using mouse PBMC isolation kit at the end of vaccine experiment. The effector memory T cells ($T_{EM}$, CD3$^+$CD8$^+$CD44$^+$CD62L$^-$) and central memory T cells ($T_{CM}$, CD3$^+$CD8$^+$CD44$^+$CD62L$^+$) were labeled with corresponding antibodies and analyzed by a flow cytometer.[50]

For analysis the cytotoxicity of memory T cells, B16-F10 cells were seeded in glass-bottom dishes for 24 h, then stained by calcein acetoxymethyl (Calcein-AM) for 30 min. PBMC were stained by Hoechst 33324 for 30 min. Then PBMCs from different group were added in the dishes and co-cultured with the B16-F10 cells for another 4 h, with the ratio of PBMCs to B16-F10 cells being 25 : 1. The tumor cell viability was measured using the calcein AM cell viability assay kit (beyotime, China) according to the manufacturer's instructions. The relative cytotoxicity = (1 − cell viability)%.

The *in vitro* visualization images were obtained under a confocal laser scanning microscope (CLSM, Carl Zeiss 880, Germany). In addition, the samples were also observed by the

scanning electron microscopy (SEM) analysis as described in the previous report.[58] Briefly, the co-culture cells were fixed in 2.5% glutaraldehyde (pH 7.4) for 2 h and postfixed with 1% osmium tetroxide. Then the samples were prepared after dehydration with sequential washes in ethanol. Afterward, the samples were sputter-coated with gold and then observed under a SEM (HITACHI, Japan).

### Statistics analysis

Data processing and statistical analysis were performed using GraphPad prism 8.0. The one-way ANOVA statistical analysis was used for comparisons between different groups. $*P < 0.05$ was considered statistically significant.

## Author contributions

Jinquan Wang and Huaiyi Huang designed all experiments; Zhongxian Fan and Li Wei synthesized and characterized the iridium complex; Yi Rong, Zhijie Yu, performed the cell and animal experiments; Han Shen and Zizhuo Zhao analyzed the data; Jinquan Wang, Huaiyi Huang, and Xiaojuan Hao wrote the manuscript. All the authors discussed the results and commented on and proofread the manuscript.

## Conflicts of interest

The authors declare no conflicts of interest.

## Acknowledgements

This work was supported by the National Natural Science Foundation of China (no. 22277013, 22277153, 22007104, 21975053), the Yin Ling Experts Projects of Guangdong Province (no. 2022A1313030043), the Natural Science Foundation of Guangdong Province (no. 2022A1515012094), Guangdong Basic and Applied Basic Research Foundation (no. 2021B1515020050), Science, Technology and Innovation Commission of Shenzhen Municipality Project (no. JCYJ20190807152616996), and the Characteristic Innovation Projects in Ordinary Colleges and Universities of Guangdong Province (no. 2021KTSCX053).

## References

1 V. M. Vorwald, D. M. Davis, R. J. Van Gulick, R. J. Torphy, J. S. Borgers, J. Klarquist, K. L. Couts, C. M. Amato, D. T. Cogswell, M. Fujita, M. J. Castleman, T. Davis, C. Lozupone, T. M. Medina, W. A. Robinson, L. Gapin, M. D. McCarter and R. P. Tobin, Circulating CD8(+) mucosal-associated invariant T cells correlate with improved treatment responses and overall survival in anti-PD-1-treated melanoma patients, *Clin. Transl. Immunol.*, 2022, **11**, e1367.

2 H. S. Duarte, C. R. P. Veiga, C. P. Veiga, A. J. A. Wainstein and A. P. Drummond-Lage, Toxicity profile of treatment with PD-1 inhibitors for lung cancer, melanoma and renal cell carcinoma: A real-world Brazilian study, *Int. Immunopharmacol.*, 2022, **108**, 108727.

3 M. K. Callahan and P. B. Chapman, PD-1 or PD-L1 blockade adds little to combination of BRAF and MEK inhibition in the treatment of BRAF V600-mutated melanoma, *J. Clin. Oncol.*, 2022, **40**, 1393–1395.

4 L. Zhou, Q. Xu, L. Huang, J. Jin, X. Zuo, Q. Zhang, L. Ye, S. Zhu, P. Zhan, J. Ren, T. Lv and Y. Song, Low-dose carboplatin reprograms tumor immune microenvironment through STING signaling pathway and synergizes with PD-1 inhibitors in lung cancer, *Cancer Lett.*, 2021, **500**, 163–171.

5 R. Mason, L. Au, A. Ingles Garces and J. Larkin, Current and emerging systemic therapies for cutaneous metastatic melanoma, *Expert Opin. Pharmacother.*, 2019, **20**, 1135–1152.

6 S. Asiry, G. Kim, P. S. Filippou, L. R. Sanchez, D. Entenberg, D. K. Marks, M. H. Oktay and G. S. Karagiannis, The cancer cell dissemination machinery as an immunosuppressive niche: a new obstacle towards the era of cancer immunotherapy, *Front. Immunol.*, 2021, **12**, 654877.

7 N. E. Donlon, R. Power, C. Hayes, J. V. Reynolds and J. Lysaght, Radiotherapy, immunotherapy, and the tumour microenvironment: Turning an immunosuppressive milieu into a therapeutic opportunity, *Cancer Lett.*, 2021, **502**, 84–96.

8 H. Arai, Y. Xiao, F. Loupakis, N. Kawanishi, J. Wang, F. Battaglin, S. Soni, W. Zhang, C. Mancao, B. Salhia, S. M. Mumenthaler, D. J. Weisenberger, G. Liang, C. Cremolini, A. Falcone, J. Millstein and H. J. Lenz, Immunogenic cell death pathway polymorphisms for predicting oxaliplatin efficacy in metastatic colorectal cancer, *J. Immunother. Cancer*, 2020, **8**, e001714.

9 F. Huang, J. Lei, Y. Sun, F. Yan, B. Chen, L. Zhang, Z. Lu, R. Cao, Y. Lin, C. Wang and G. Tan, Induction of enhanced immunogenic cell death through ultrasound-controlled release of doxorubicin by liposome-microbubble complexes, *OncoImmunology*, 2018, **7**, e1446720.

10 B. Du and D. J. Waxman, Medium dose intermittent cyclophosphamide induces immunogenic cell death and cancer cell autonomous type I interferon production in glioma models, *Cancer Lett.*, 2020, **470**, 170–180.

11 M. Jiang, J. Zeng, L. Zhao, M. Zhang, J. Ma, X. Guan and W. Zhang, Chemotherapeutic drug-induced immunogenic cell death for nanomedicine-based cancer chemo-immunotherapy, *Nanoscale*, 2021, **13**, 17218–17235.

12 D. V. Krysko, A. D. Garg, A. Kaczmarek, O. Krysko, P. Agostinis and P. Vandenabeele, Immunogenic cell death and DAMPs in cancer therapy, *Nat. Rev. Cancer*, 2012, **12**, 860–875.

13 Q. Duan, H. Zhang, J. Zheng and L. Zhang, Turning cold into hot: firing up the tumor microenvironment, *Trends Cancer*, 2020, **6**, 605–618.

 

14 K. Kersten, C. Salvagno and K. E. de Visser, Exploiting the immunomodulatory properties of chemotherapeutic drugs to improve the success of cancer immunotherapy, *Front. Immunol.*, 2015, **6**, 516.
15 M. Sereno, O. Higuera, P. Cruz Castellanos, S. Falagan, X. Mielgo-Rubio, J. C. Trujillo-Reyes and F. Counago, Immunotherapy combinations and chemotherapy sparing schemes in first line non-small cell lung cancer, *World J. Clin. Oncol.*, 2021, **12**, 1182–1192.
16 D. Salas-Benito, J. L. Perez-Gracia, M. Ponz-Sarvise, M. E. Rodriguez-Ruiz, I. Martinez-Forero, E. Castanon, J. M. Lopez-Picazo, M. F. Sanmamed and I. Melero, Paradigms on immunotherapy combinations with chemotherapy, *Cancer Discovery*, 2021, **11**, 1353–1367.
17 S. Sen, M. Won, M. S. Levine, Y. Noh, A. C. Sedgwick, J. S. Kim, J. L. Sessler and J. F. Arambula, Metal-based anticancer agents as immunogenic cell death inducers: the past, present, and future, *Chem. Soc. Rev.*, 2022, **51**, 1212–1233.
18 S. Meltzer, E. Kalanxhi, S. Dueland, K. Flatmark, K. R. Redalen and A. H. Ree, Oxaliplatin-induced immune factors and long-term disease control in rectal cancer - a reflection of immunogenic tumor cell death, *Cancer Res.*, 2016, **76**, 4006.
19 V. Novohradsky, J. Pracharova, J. Kasparkova, C. Imberti, H. E. Bridgewater, P. J. Sadler and V. Brabec, Induction of immunogenic cell death in cancer cells by a photoactivated platinum(IV) prodrug, *Inorg. Chem. Front.*, 2020, **7**, 4150–4159.
20 M. J. R. Tham, M. V. Babak and W. H. Ang, PlatinER: a highly potent anticancer platinum(II) complex that induces endoplasmic reticulum stress driven immunogenic cell death, *Angew. Chem., Int. Ed.*, 2020, **59**, 19070–19078.
21 K. Huang, F. Wang, H. Feng, H. Luo, Y. Long, T. Zou, A. S. C. Chan, R. Liu, H. Zou, Z. Chen, Y. Liu, Y. Liu and H. Liang, An aminophosphonate ester ligand-containing platinum(II) complex induces potent immunogenic cell death in vitro and elicits effective anti-tumour immune responses in vivo, *Chem. Commun.*, 2019, **55**, 13066–13069.
22 D. Wong, W. Ong and W. Ang, Induction of immunogenic cell death by chemotherapeutic platinum complexes, *Angew. Chem., Int. Ed.*, 2015, **54**, 6483–6487.
23 D. Wei, Y. Huang, B. Wang, L. Ma, J. Karges and H. Xiao, Photo-reduction with NIR light of nucleus-targeting Pt(IV) nanoparticles for combined tumor-targeted chemotherapy and photodynamic immunotherapy, *Angew. Chem., Int. Ed.*, 2022, **61**, e202201486.
24 F. Wei, L. Ke, S. Gao, J. Karges, J. Wang, Y. Chen, L. Ji and H. Chao, In situ oxidative polymerization of platinum(IV) prodrugs in pore-confined spaces of $CaCO_3$ nanoparticles for cancer chemoimmunotherapy, *Chem. Sci.*, 2023, **14**(25), 7005–7015.
25 P. Konda, J. A. Roque III, L. M. Lifshits, A. Alcos, E. Azzam, G. Shi, C. G. Cameron, S. A. McFarland and S. Gujar, Photodynamic therapy of melanoma with new, structurally similar, NIR-absorbing ruthenium(II) complexes promotes tumor growth control via distinct hallmarks of immunogenic cell death, *Am. J. Cancer Res.*, 2022, **12**, 210–228.
26 P. Konda, L. M. Lifshits, J. A. Roque 3rd, H. D. Cole, C. G. Cameron, S. A. McFarland and S. Gujar, Discovery of immunogenic cell death-inducing ruthenium-based photosensitizers for anticancer photodynamic therapy, *OncoImmunology*, 2020, **10**, 1863626.
27 D. Wernitznig, K. Kiakos, G. Del Favero, N. Harrer, H. Machat, A. Osswald, M. A. Jakupec, A. Wernitznig, W. Sommergruber and B. K. Keppler, First-in-class ruthenium anticancer drug (KP1339/IT-139) induces an immunogenic cell death signature in colorectal spheroids in vitro, *Metallomics*, 2019, **11**, 1044–1048.
28 L. M. Lifshits, J. A. Roque III, P. Konda, S. Monro, H. D. Cole, D. von Dohlen, S. Kim, G. Deep, R. P. Thummel, C. G. Cameron, S. Gujar and S. A. McFarland, Near-infrared absorbing Ru(ii) complexes act as immunoprotective photodynamic therapy (PDT) agents against aggressive melanoma, *Chem. Sci.*, 2020, **11**, 11740–11762.
29 S. Ji, X. Yang, X. Chen, A. Li, D. Yan, H. Xu and H. Fei, Structure-tuned membrane active Ir-complexed oligoarginine overcomes cancer cell drug resistance and triggers immune responses in mice, *Chem. Sci.*, 2020, **11**, 9126–9133.
30 L. Wang, R. Guan, L. Xie, X. Liao, K. Xiong, T. W. Rees, Y. Chen, L. Ji and H. Chao, An ER- targeting iridium(III) complex that induces immunogenic cell death in non-small-cell lung cancer, *Angew. Chem., Int. Ed.*, 2021, **60**, 4657–4665.
31 L. Wang, J. Karges, F. Wei, L. Xie, Z. Chen, G. Gasser, L. Ji and H. Chao, A mitochondria-localized iridium(III) photosensitizer for two-photon photodynamic immunotherapy against melanoma, *Chem. Sci.*, 2023, **14**, 1461–1471.
32 W. Wang, Y. Ling, Y. Zhong, Z. Li, C. Tan and Z. Mao, Ferroptosis- enhanced cancer immunity by a ferrocene-appended iridium(III) diphosphine complex, *Angew. Chem., Int. Ed.*, 2022, **61**, e202115247.
33 X. Xiong, K. Huang, Y. Wang, B. Cao, Y. Luo, H. Chen, Y. Yang, Y. Long, M. Liu, A. S. C. Chan, H. Liang and T. Zou, Target profiling of an iridium(III)-based immunogenic cell death inducer unveils the engagement of unfolded protein response regulator BiP, *J. Am. Chem. Soc.*, 2022, **144**, 10407–10416.
34 G. Vigueras, L. Markova, V. Novohradsky, A. Marco, N. Cutillas, H. Kostrhunova, J. Kasparkova, J. Ruiz and V. Brabec, A photoactivated ir(iii) complex targets cancer stem cells and induces secretion of damage-associated molecular patterns in melanoma cells characteristic of immunogenic cell death, *Inorg. Chem. Front.*, 2021, **8**, 4696–4711.
35 N. Xu, A. Hu, X. Pu, J. Wang, X. Liao, Z. Huang and G. Yin, Cu-chelated polydopamine nanoparticles as a photothermal medium and "immunogenic cell death" inducer for combined tumor therapy, *J. Mater. Chem. B*, 2022, **10**, 3104–3118.

36 R. D. Mule, A. Kumar, S. P. Sancheti, B. Senthilkumar, H. Kumar and N. T. Patil, BQ-AurIPr: a redox-active anticancer Au(i) complex that induces immunogenic cell death, *Chem. Sci.*, 2022, **13**, 10779–10785.

37 S. Sen, S. Hufnagel, E. Y. Maier, I. Aguilar, J. Selvakumar, J. E. DeVore, V. M. Lynch, K. Arumugam, Z. Cui, J. L. Sessler and J. F. Arambula, Rationally designed redox-active Au(I) N-heterocyclic carbene: an immunogenic cell death inducer, *J. Am. Chem. Soc.*, 2020, **142**, 20536–20541.

38 L. Zhang, N. Montesdeoca, J. Karges and H. Xiao, Immunogenic cell death inducing metal complexes for cancer therapy, *Angew. Chem., Int. Ed.*, 2023, **62**, e202300662.

39 J. Wang, H. Zhang, X. Yin and Y. Bian, Oxaliplatin induces immunogenic cell death in human and murine laryngeal cancer, *J. Oncol.*, 2022, **2022**, 3760766.

40 G. L. Plosker, C. M. Perry and K. L. Goa, Efavirenz: a pharmacoeconomic review of its use in HIV infection, *PharmacoEconomics*, 2001, **19**, 421–436.

41 W. Wu, J. Sigmond, G. J. Peters and R. F. Borch, Synthesis and biological activity of a gemcitabine phosphoramidate prodrug, *J. Med. Chem.*, 2007, **50**, 3743–3746.

42 J. M. Nelson, T. M. Chiller, J. H. Powers and F. J. Angulo, Fluoroquinolone-resistant campylobacter species and the withdrawal of fluoroquinolones from use in poultry: a public health success story, *Clin. Infect. Dis.*, 2007, **44**, 977–980.

43 R. Hanayama, H. Shimizu, H. Nakagami, M. K. Osako, H. Makino, Y. Kunugiza, T. Tomita, I. Tsukamoto, H. Yoshikawa, H. Rakugi and R. Morishita, Fluvastatin improves osteoporosis in fructose-fed insulin resistant model rats through blockade of the classical mevalonate pathway and antioxidant action, *Int. J. Mol. Med.*, 2009, **23**, 581–588.

44 Z. Fan, J. Xie, T. Sadhukhan, C. Liang, C. Huang, W. Li, T. Li, P. Zhang, S. Banerjee, K. Raghavachari and H. Huang, Highly efficient ir(III)-coumarin photo-pedox catalyst for synergetic multi-mode cancer photo-therapy, *Chem. – Eur. J.*, 2022, **28**, e202103346.

45 J. Wang, P. Zhang, C. Qian, X. Hou, L. Ji and H. Chao, Mitochondria are the primary target in the induction of apoptosis by chiral ruthenium(II) polypyridyl complexes in cancer cells, *J. Biol. Inorg. Chem.*, 2014, **19**, 335–348.

46 A. D. Garg, D. V. Krysko, P. Vandenabeele and P. Agostinis, Extracellular ATP and $P_2X_7$ receptor exert context-specific immunogenic effects after immunogenic cancer cell death, *Cell Death Dis.*, 2016, **7**, 3.

47 I. Martins, Y. Wang, M. Michaud, Y. Ma, A. Q. Sukkurwala, S. Shen, O. Kepp, D. Metivier, L. Galluzzi, J. L. Perfettini, L. Zitvogel and G. Kroemer, Molecular mechanisms of ATP secretion during immunogenic cell death, *Cell Death Differ.*, 2014, **21**, 79–91.

48 M. Kielbik, I. Szulc-Kielbik and M. Klink, Calreticulin- multifunctional chaperone in immunogenic cell death: potential significance as a prognostic biomarker in ovarian cancer patients, *Cells*, 2021, **10**, 130.

49 A. T. H. Selno, S. Schlichtner, I. M. Yasinska, S. S. Sakhnevych, W. Fiedler, J. Wellbrock, S. M. Berger, E. Klenova, B. F. Gibbs, E. Fasler-Kan and V. V. Sumbayev, High mobility group box 1 (HMGB1) induces toll-like receptor 4-mediated production of the immunosuppressive protein galectin-9 in human cancer cells, *Front. Immunol.*, 2021, **12**, 675731.

50 Y. Guo, S. Wang, X. Zhang, H. Jia, Y. Zhu, X. Zhang, G. Gao, Y. Jiang, C. Li, X. Chen, S. Wu, Y. Liu and F. Wu, In situ generation of micrometer-sized tumor cell-derived vesicles as autologouscancer vaccines for boosting systemic immune responses, *Nat. Commun.*, 2022, **13**, 6534.

51 Z. Zhao, K. Qiu, J. Liu, X. Hao and J. Wang, Two-photon photodynamic ablation of tumour cells using an RGD peptide-conjugated ruthenium(II) photosensitiser, *Chem. Commun.*, 2020, **56**, 12542–12545.

52 L. Huang, Y. Li, Y. Du, Y. Zhang, X. Wang, Y. Ding, X. Yang, F. Meng, J. Tu, L. Luo and C. Sun, Mild photothermal therapy potentiates anti-PD-L1 treatment for immunologically cold tumors via an all-in-one and all-in-control strategy, *Nat. Commun.*, 2019, **10**, 4871.

53 J. Wang, P. Zhang, C. Qian, X. Hou, L. Ji and H. Chao, Mitochondria are the primary target in the induction of apoptosis by chiral ruthenium(II) polypyridyl complexes in cancer cells, *J. Biol. Inorg. Chem.*, 2014, **19**, 335–348.

54 H. Zhou, C. Tu, P. Yang, J. Li, O. Kepp, H. Li, L. Zhang, L. Zhang, Y. Zhao, T. Zhang, C. Sheng and J. Wang, Carbon ion radiotherapy triggers immunogenic cell death and sensitizes melanoma to anti-PD-1 therapy in mice, *OncoImmunology*, 2022, **11**, 2057892.

55 D. Chen, S. Guo, X. Tang, Y. Rong, H. Bo, H. Shen, Z. Zhao, A. Iao, J. Shen and J. Wang, Combination of ruthenium(II) polypyridyl complex delta-Ru1 and taxol enhances the anticancer effect on taxol-resistant cancer cells through Caspase-1/GSDMD-mediated pyroptosis, *J. Inorg. Biochem.*, 2022, **230**, 111749.

56 Z. Zhao, J. Wu, X. Liu, M. Liang, X. Zhou, S. Ouyang, J. Yao, J. Wang and B. Luo, Insufficient radiofrequency ablation promotes proliferation of residual hepatocellular carcinoma via autophagy, *Cancer Lett.*, 2018, **421**, 73–81.

57 B. Kwong, H. Liu and D. J. Irvine, Induction of potent anti-tumor responses while eliminating systemic side effects via liposome-anchored combinatorial immunotherapy, *Biomaterials*, 2011, **32**, 5134–5147.

58 A. Nanou, M. Crespo, P. Flohr, J. S. De Bono and L. Terstappen, Scanning electron microscopy of circulating tumor cells and tumor-derived extracellular vesicles, *Cancers*, 2018, **10**, 416.

 